*Article*

# Assessment of the Additive Fabrication Quality of Sandwich Structures with Novel Triply Periodic Minimal Surface Cores

Alexandru Vasile [1,2], Dan Mihai Constantinescu [1,3,*], Iulian Constantin Coropețchi [1,2], Ștefan Sorohan [1] and Dragoș Alexandru Apostol [1]

1    Department of Strength of Materials, National University for Science and Technology Politehnica Bucharest, Splaiul Independeţei 313, 060042 Bucharest, Romania; alexandru.vasile@mta.ro (A.V.); iulian.coropetchi@mta.ro (I.C.C.); stefan.sorohan@upb.ro (Ș.S.); dragos.apostol@upb.ro (D.A.A.)

2    Faculty of Aircraft and Military Vehicles, Military Technical Academy "Ferdinand I", G. Coşbuc Blvd. 39-49, 050141 Bucharest, Romania

3    Technical Sciences Academy of Romania, Dacia Blvd. 26, 030167 Bucharest, Romania

*    Correspondence: dan.constantinescu@upb.ro

**Abstract:** Triply periodic minimal surface (TPMS) structures raised significant interest in several areas of research due to their unique properties and broad range of applications. The aim of the paper is to verify if such complex metamaterials can be fabricated effectively without defects that could compromise their mechanical response. An implicit modeling approach was used to generate eight novel TPMS structures and one stochastic topology. Multiple specimens were fabricated from a photopolymeric resin using a stereolithography (SLA) technique, and an analysis of the manufactured samples was carried out in terms of surface quality, dimensional and mass deviations, and internal porosity of the material. Laser scanning showed no significant deviations from the designed geometry but highlighted errors during the post-processing stages of manufacturing. Surface analysis resulted in an average roughness of 2.47 μm, a value specific to well-controlled additive manufacturing (AM) techniques. A microscopic examination portrays common types of defects, while an ultrasonic non-destructive inspection method showed no indication of defects in the depth of the samples. Sectioning the samples through water jet cutting exposed interior surfaces with better homogeneity than the exterior ones and the absence of a layer-by-layer aspect. Overall, the samples displayed no major defects and good accuracy, with minor inconsistencies and methods of mitigating them having been presented.

**Keywords:** TPMS; implicit modeling; dimensional verification; quality control

## 1. Introduction

In recent relevant literature publications, significant interest has been directed towards the investigation of triply periodic minimal surface (TPMS) structures fabricated through additive manufacturing (AM) techniques [1–5]. The results indicate that such structures present superior properties compared to conventional equivalent topologies in terms of modulus of elasticity, compressive strength, and energy absorption capacity and may have practical applications in fields such as automotive or medical industries [6–8]. Among these structures, thin-walled geometries offer higher predictability in terms of mechanical response compared to "strut-based" structures. At the same time, the "shell-based" structures, on which this research is based, created thin walls around a surface defined by a mathematical function, offering thus a higher strength-to-mass ratio than the "skeleton-based" structures, which are built by separating the domain in two volumes, delimited by the mathematical function [3,9].

A detailed presentation of TPMS geometries was conducted in [10], highlighting geometry design algorithms and performance control strategies, AM methods typically

used, and multidisciplinary applications to identify the advantages and real potential of such structures, but also the problems and existing challenges.

Publications on TPMS structures show, however, a disproportionate interest in understanding the behavior and printing accuracy of already defined geometries such as Gyroid [11–14], Diamond [15,16], Schwarz [17,18], Lidinoid [19], Neovius [20,21], and Split-P [22]. Thus, little interest is directed towards developing new topologies in order to obtain superior properties. This paper aims to present eight novel TPMS structures and one stochastic geometry, architected through implicit modeling and fabricated through an SLA method.

Since comparison between already mature geometries and novel designs can only be achieved by the characterization of the mechanical response and resulting properties, it is imperative to verify that the mechanical behavior is not heavily influenced by manufacturing defects. This is especially important in small-scale complex tri-dimensional topologies, which are susceptible to fabrication irregularities.

In the AM of complex structures, common defects include porosity, residual stresses, warping, and surface roughness. Porosity often results from insufficient melting, gas entrapment, impurities, or vaporization of alloying elements, leading to reduced mechanical properties. Residual stresses arise due to rapid thermal cycling during layer formation or deposition, which can cause warping, cracking, distortion, or delamination. Additionally, uneven cooling may result in dimensional inaccuracies. Surface roughness, influenced by layer thickness and particle size, impacts post-processing requirements and part performance [23–25].

To minimize defects in AM parts, several techniques are employed, including optimizing process parameters, post-processing, and in-situ monitoring [26]. Process optimization focuses on adjusting laser power, refining resin or powder quality, environmental control (e.g., oxygen level or material temperature), and optimizing layer thickness to ensure uniform melting, solidification, reduced porosity, and warping [27,28]. Post-processing techniques, such as heat or radiation treatment, can relieve residual stresses and improve material properties. In-situ monitoring systems, incorporating sensors and machine learning, help detect defects and enable corrective actions in real-time [29].

Validating that an AM technique is suitable for a given topology involves answering several challenges. Thus, an analysis of the fabrication precision of the chosen SLA method was conducted, and different methods for assessing the quality of the proposed specimens are presented.

In the present research, a careful dimensional deviation analysis, a surface roughness analysis, and a visual inspection were performed to determine if the chosen manufacturing process is suitable for the proposed TPMS-designed geometries. A supplementary investigation was undertaken to observe the possible internal defects of the specimens by using ultrasonic non-destructive testing.

Future work includes low-velocity impact characterization of the specimens and creating a framework to integrate implicit geometries modeling into finite element analyses. These simulations should faithfully recreate the deformation mechanism of the samples, which, depending on the identified manufacturing flaws, may involve integrating different types of fabrication defects in the finite element model, as conducted in [30,31].

## 2. Materials and Methods

### 2.1. Sample Design

The vast majority of tools for designing novel topologies of materials make use of traditional computer-aided design (CAD) software. They use boundary representation methods (B-reps), which are topology details that define the connectivity between faces, edges, and vertices. This method, although used on a large scale, is difficult to implement if the imagined geometries have a high degree of complexity or can only be defined by mathematical functions difficult to approximate using simple shapes.

Implicit modeling is a technique of defining and representing three-dimensional topologies, where the geometry is described by an equation or set of equations rather than a network of vertices, edges, and faces. The principle that describes the creation of functional parts using implicit modeling is that an implicit mathematical function returns negative values for any point in three-dimensional space that is inside the considered solid, positive values when that point is outside the solid, and zero function value if the point is on its contour. Also, because it avoids the discretization process used in CAD methods, there is no risk that the meshing accuracy does not faithfully capture the continuity of the solid, resulting in a geometry that is easier to calculate, and having a pure shape. Avoiding discretization in the process of creating the geometry does not exclude its necessity in the stages of the simulation or preparation of the AM processes, but it helps to substantially reduce the computational effort and the sizes of the resulting files.

The two software packages that were used in this paper are NTopology v4.5.3 and TPMS Designer v3.2.1.2. NTopology is commercial software that allows implicit design to be used for modeling, simulation, and processing parts for AM. It benefits from comprehensive documentation and allows generation, visualization, and export of geometries in various forms. It has predefined a number of representative cell types but also offers the possibility of building novel configurations. The software provides parametric modeling capabilities, flexibility in the design iteration process, assistance in preparing parts for fabrication, topology optimization components, organization methods in the form of personalized and collaborative workflows, and simulation components for the determination of mechanical and thermal performances [32]. TPMS Designer is a library developed to be used in Matlab that, in addition to the benefits brought by the advantages of the implicit geometry, also allows a more detailed and customized analysis of newly developed geometries. In addition, it provides an overview of some parameters used to analyze the performance of artificial structures and insights into applicable manufacturing constraints [33].

The mathematical formulations, Equations (2)–(9), of the eight novel TPMS proposed structures, together with the gyroid given by Equation (1), are presented in Table 1. The principles that guided the definition of these equations are that the topologies should be self-supported because any internal supports needed during fabrication would not allow for easy scaling or would alter the mechanical response of the structure. They should also be novel designs, geometrically different from each other, in order to capture various mechanical responses. Moreover, no enclosed chambers should be generated where resin or powder can remain stored during manufacturing.

**Table 1.** Mathematical definitions of the proposed TPMS topologies.

| Sample | Definition [34] | Eq. |
|---|---|---|
| S1 (gyroid) | $f(x,y,z) = \cos(x) \times \sin(y) + \cos(y) \times \sin(z) + \cos(z) \times \sin(x)$ | (1) |
| S2 | $f(x,y,z) = 2 \times [\cos(x) \times \cos(y) + \cos(y) \times \cos(z) + \cos(z) \times \cos(x)] - [\cos(2x) + \cos(2y) + \cos(2z)]$ | (2) |
| S3 | $f(x,y,z) = \cos(x) \times \cos(y) + \cos(x) \times \cos(z) + \cos(y) \times \cos(z) + \sin(x) \times \cos(y) + \sin(x) \times \cos(z) + \sin(y) \times \cos(z) + \sin(y) \times \cos(z) + \sin(z) \times \cos(x) + \sin(z) \times \cos(y)$ | (3) |
| S4 | $f(x,y,z) = \cos(2x) \times \cos(y) \times \cos(z) + \cos(2y) \times \cos(x) \times \cos(z) + \cos(2z) \times \cos(x) \times \cos(y) + \sin(x) \times \cos(y) + \sin(x) \times \cos(z) + \sin(y) \times \cos(z) + \sin(y) \times \cos(z) + \sin(z) \times \cos(x) + \sin(z) \times \cos(y)$ | (4) |
| S5 | $f(x,y,z) = \sin(x) \times \cos(y) \times z/2 + \sin(y) \times \cos(z) \times x/2 + \sin(z) \times \cos(x) \times y/2$ | (5) |
| S6 | $f(x,y,z) = 4 \times \cos(x) \times \cos(y) \times \cos(z) - [\cos(2x) \times \cos(2y) + \cos(2y) \times \cos(2z) + \cos(2z) \times \cos(2x)]$ | (6) |
| S7 | $f(x,y,z) = 4 \times \sin(x) \times \cos(y) \times \cos(z) - [\cos(x) \times \cos(y) + \cos(y) \times \cos(z) + \cos(z) \times \cos(x)]$ | (7) |
| S8 | $f(x,y,z) = 8 \times \cos(x/2) \times \cos(z/2) \times \sin(x/2) + 8 \times \cos(y/2) \times \cos(z/2) \times \sin(y/2) + 8 \times \cos(x/2) \times \cos(y/2) \times \sin(z/2)$ | (8) |
| S9 | $f(x,y,z) = \sin(x) \times \sin(y) + \sin(x) \times \sin(y) + \sin(x) \times \sin(y) - 4 \times \cos(x) \times \cos(y) \times \cos(z)$ | (9) |

Starting from the graphical visualization of the contour defined by these equations (the gyroid representative volume element (RVE) acting as a reference in Figure 1a), two symmetrical surfaces were generated (Figure 1b) to delimit the volume of the created "sheet-based" cell (Figure 1c). The distance between the two surfaces gives the thickness of the walls, which was varied in order to maintain a relative density of 0.3 across all the proposed topologies.
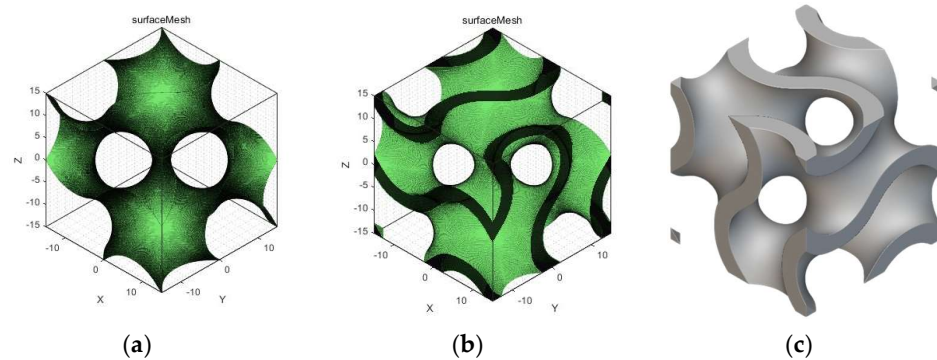


(**a**)  (**b**)  (**c**)

**Figure 1.** (**a**) Fundamental surface, (**b**) Boundary surfaces, (**c**) Solid reference volume element of metamaterials (gyroid type).

### 2.2. Sample Fabrication

Sandwich specimens were created with 3 mm thick face sheets, incorporating TPMS cores made out of 27 (3 × 3 × 3) 10 mm RVEs inside a 30 mm cube shape. The 10th sample has a stochastic strut-based definition with the same relative density. It was constrained so that the ligaments followed a direction perpendicular to the sheets, with an average distance between them of 3.5 mm and an average number of six struts intersecting at the same point. All the topologies are displayed in Figure 2a.
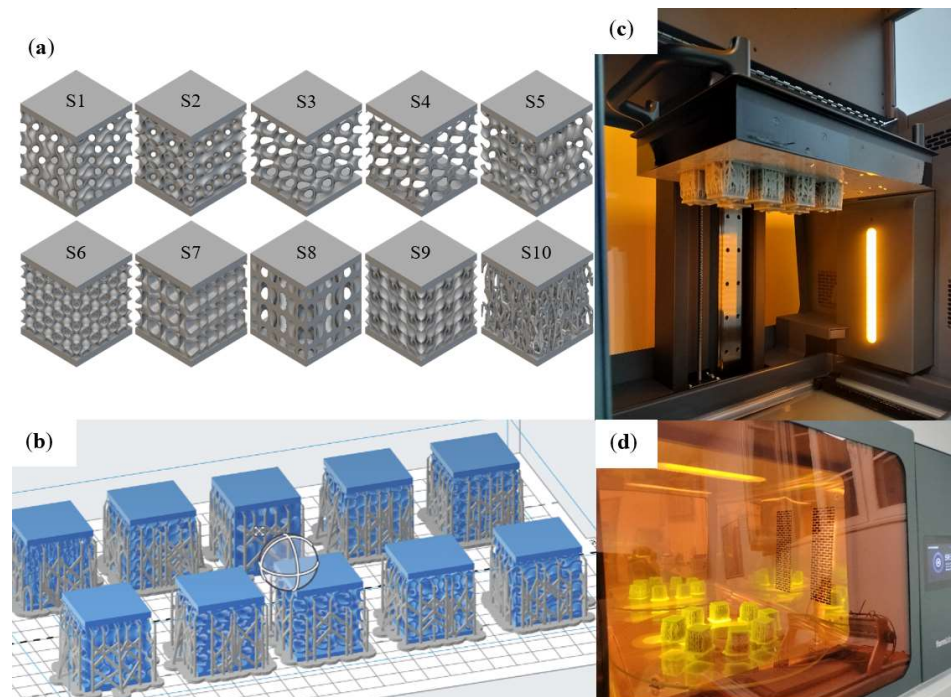


**Figure 2.** (**a**) Topology of the proposed specimens; (**b**) Sample preparation for additive manufacturing; (**c**) SLA printing; (**d**) UV curing of the specimens.

Given the complex geometry of the topologies, a fabrication method that offers high precision was necessary, as it would ideally result in a very small number of defects. Thus, an SLA technique was employed on a Form 3L printer (Formlabs, Somerville, MA, USA) using a photosensitive resin commercially available as Tough 1500 v1 (Formlabs, Somerville, MA, USA).

AM preparation of the models was performed in the dedicated Preform software 3.42.1. A discretization of 25 μm was used for transforming the implicit model into a format suitable for being used in AM, standard tessellation language (stl.). This value was chosen to be in accordance with the minimal printable layer thickness of 50 μm that was used. Since the lateral boundaries of the samples can lead to areas that do not provide sufficient printing support, lateral supports were added to allow for successful fabrication. Their density was reduced to 50% of the sample's density, and the point of contact with the part was defined at 0.35 mm to facilitate subsequent removal without damaging the surfaces.

Various ways of orienting and positioning the samples and support elements were tried so that no visible deviations from the nominal geometry of the parts would occur. Figure 2b shows the method chosen as optimal, directly on the printing table, without suspending the parts on supports, to reduce the risk of defects due to their insufficiency. Special attention was directed towards not positioning the parts on the longitudinal axis of symmetry of the table, because in this case both laser beams would have been used for the same sample, and inhomogeneity defects could appear in the joining area. In order to minimize defect probability, all 10 samples were printed together from the same batch of resin, resulting in a specific printing time of 3.38 min/mL, while printing a single part would amount to 15.23 min/mL. Figure 2c presents the samples immediately after SLA printing.

Post-processing involved using standard washing programs to remove residual resin from the specimens. This step was carried out automatically on all the samples at the same time in a Form Wash L (Formlabs, Somerville, MA, USA) unit, using isopropyl alcohol. Next, Figure 2d portrays the parts being cured together in a reflective Form Cure (Formlabs, Somerville, MA, USA) enclosure, using a 70 °C temperature environment and ultraviolet radiation with a wavelength of 350 nm for 1 h. The only manual intervention was to remove the lateral supports of the specimens. Figure 3 shows all the specimens after the entire fabrication process.
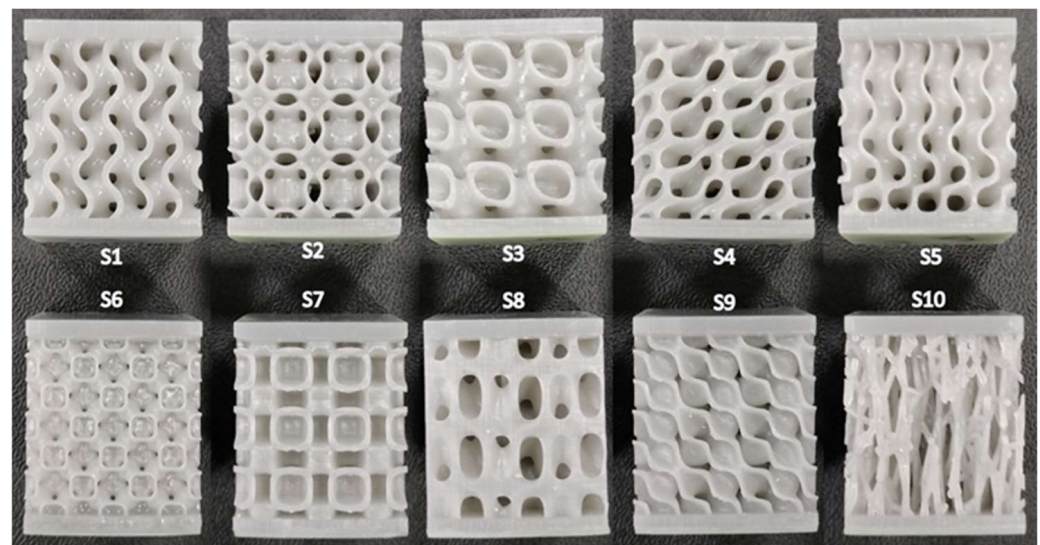


**Figure 3.** All the printed samples.

## 2.3. Fabrication Analysis

The first step in controlling the manufacturing process and a good indicator of defects in fabricated parts is to verify their weight. A digital precision scale, Kern PF8-2000 (Kern and Sohn, Albstadt, Germany), with a precision of 0.01 g was used.

Implicit modeling allows for accurately determining the volume of the topologies. The density inserted in the nTopology v4.5.3 software was selected as the resulting mass will match the average mass value determined after weighing all the samples. This led to a deviation between the chosen density of the polymer of 0.00107 g/mm$^3$ and the actual density of 0.00121 g/mm$^3$.

In order to study the dimensional deviations, a tri-dimensional (3D) scanning method was used. This involved using a Hexagon Absolute Arm 7-Axis scanner (Hexagon AB, Stockholm, Sweden) and comparing the resulting point cloud with the CAD model. The setup of the scanning device and the operating mode can be identified in Figure 4. Once the orientation and alignment were verified to be correct with predefined nominal geometry, the point cloud was generated by scanning the part with an AS1 scanner with a resolution of 0.016 mm, an acquisition rate of up to 1.2 million points/s, and a minimum point spacing of 0.027 mm. The scan was made from several passes with different tilt angles of the scan head, obtaining a cloud of more than 9 million points.



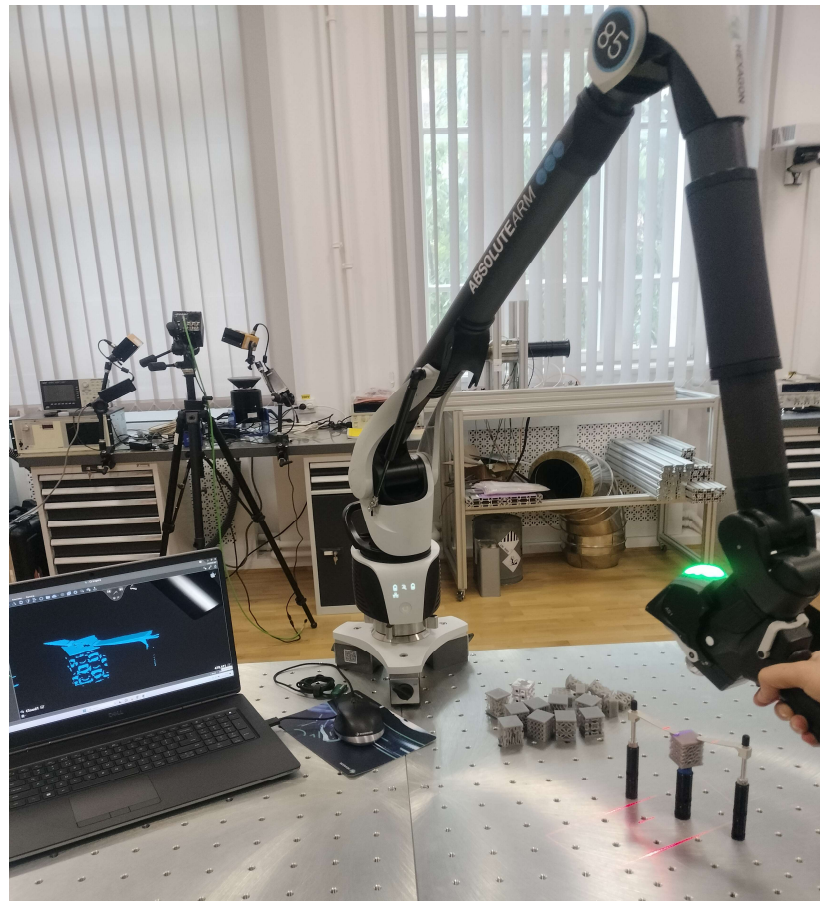**Figure 4.** Setup for 3D scanning using a Hexagon Absolute Arm 7-Axis scanner.

A roughness analysis was performed using a Surtronic S-100 (Taylor Hobson, Leicester, UK) portable roughness meter. The measured profile resulted from scanning the actual profile with a 5 μm probe, which captured surface imperfections such as cracks, scratches, voids, or excess material. The measuring procedure is displayed in Figure 5.

**Figure 5.** Setup for roughness determination using Surtronic S128.

Three different surfaces were measured: the bottom surface, to inspect if defects appear when the samples are detached from the build plate; the upper surface, to observe if the surface most exposed to external factors can undergo deformations before the curing process; the sidewalls, to observe whether the layer-by-layer appearance translates into high roughness. The measurements were carried out at a distance of 8 mm with a 0.4 mm pass filter at a speed of 1 mm/s with 5 passes for each type of surface, and each sample was analyzed.

To verify the values obtained with the roughness probe and to identify surface defects, a visual inspection was also performed on a Keyence VHX-7100 (Keyence, Tokyo, Japan) microscope.

To verify specimen homogeneity, a non-destructive measurement method using ultrasound was used. A thickness and depth defect measuring device, Sonowall 50 (Sonotec, Halle, Germany), was used with the following measurement parameters: 10 μm resolution, 2400 m/s ultrasound speed specific to plastic materials, SW 5-21 5 Mhz probe. Due to the complicated geometry of the parts and the dimensions of the ultrasonic probe, the measurement could only be successfully performed on the upper and lower faces of the sandwich specimens. To further test the homogeneity of the printed parts, type I tensile specimens, configured according to the ASTM D638 standard and fabricated through the same procedure, were also verified. The specimens were fabricated for material properties validation and laid flat on the platform during printing, with the build direction along their thickness. An image taken during an inspection is shown in Figure 6a.
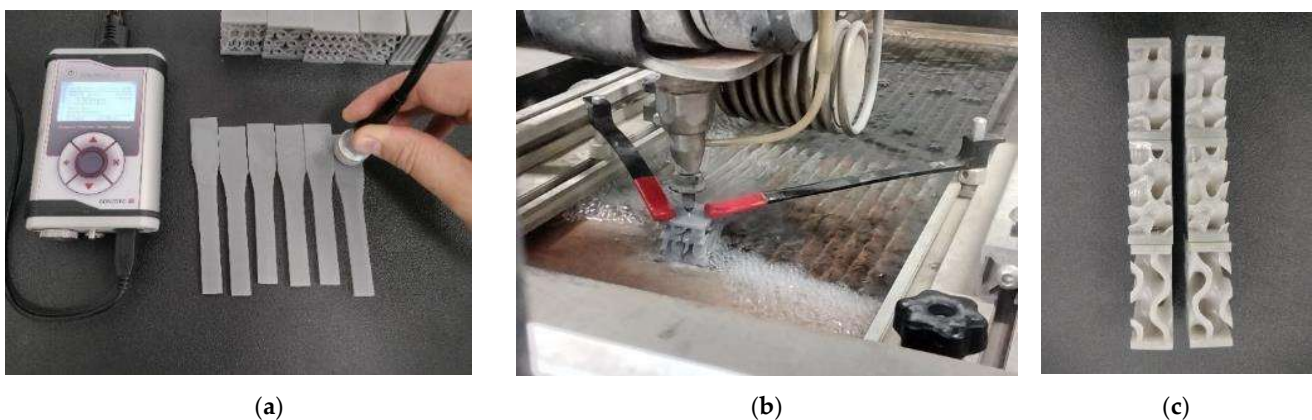


(**a**) (**b**) (**c**)

**Figure 6.** (**a**) Thickness and internal defect detection using ultrasounds; (**b**) Image during water jet cutting; (**c**) Cut samples.

All flat surfaces that allow the positioning of the probe were analyzed, aiming to identify situations where the identified thickness is significantly different from the nominal one, which would indicate the presence of voids or porosities.

To verify the cross-section aspect of the samples, a water jet cutting process was employed with a 0.5 mm nozzle, visible in Figure 6b, to minimize the damage to the exposed surfaces. This resulted in the samples presented in Figure 6c. After cutting the samples, an analysis of the cores of the specimens was also performed through a similar microscopic inspection. This was performed for both the lateral surfaces of the sample and the newly exposed surfaces.

## 3. Results

Studies examining the effects of defects on the mechanical properties of structures concluded that defects have a significant impact on the mechanical response of AM parts [35]. This underlines the need for careful analysis and more stringent control over the fabrication process.

Probably the biggest disadvantage specific to additive manufacturing is the lack of isotropy and homogeneity of the printed structures. This materializes in the presence of air voids between the layers of material, especially due to non-uniformities in surface temperature, material melting/polymerization temperature, impurities, or water absorption, and can lead to lower mechanical properties.

Although technologies based on photopolymerization have a higher degree of precision than those based on material extrusion and are less subjected to the occurrence of such major manufacturing defects [36,37], a detailed analysis of the manufactured samples was necessary in order to have an indication of the possible errors. This is necessary in order to consider corrective methods that shall minimize the defects or allow for bigger deviations between the experimental and simulation data if such an endeavor is desired. Next, the methods through which qualitative and quantitative analyses of the manufactured samples were performed are presented in detail.

### 3.1. Mass Verification

The results obtained through weighting the samples are presented in Table 2. While the error is low for most samples, specimen S6 presented a significant deviation of almost 4%. This was due to the very small features of the topology, which ensures a superior total external surface. This, in turn, provides a higher probability of obtaining residual resin and requires an adjusted washing procedure to ensure proper post-processing. As such, the samples need to be post-processed separately and leave a bigger space between them when being positioned on the printing table in order to allow the alcohol to properly wash the internal chambers of the specimens. Another reason for the appearance of mass deviations between samples is the geometry of the part itself. Some samples present, at the level of the outer contour, separate areas without support, which will not be considered at the time of AM. Most of the time, they are insignificant in mass. Their minimization can be carried out by changing the range of the function that defines the part or by the subsequent rotation of the representative cell around an axis. It must be acknowledged that the latter choice would lead to other types of mechanical behaviors since the geometries are not isotropic.

**Table 2.** Mass of printed samples.

|  | S1 | S2 | S3 | S4 | S5 | S6 | S7 | S8 | S9 | S10 |
|---|---|---|---|---|---|---|---|---|---|---|
| Sample mass [g] | 16.55 | 17.05 | 17.19 | 17.14 | 16.49 | 17.50 | 16.73 | 16.45 | 16.83 | 16.40 |
| Average | | | | | 16.833 | | | | | |
| Relative error [%] | 1.68 | −1.29 | −2.12 | −1.82 | 2.04 | −3.96 | 0.61 | 2.28 | 0.02 | 2.57 |

### 3.2. Dimensional Deviation Analysis

One point cloud determined while scanning the samples is presented as a reference in the image shown in Figure 7a for topologies S1 and S8. After removing the points not relevant to the part, comparing the position of the points with the nominal dimensions of the specimen, and applying a tolerance of ±0.1 mm, the results highlighted in Figure 7b,c were obtained. S1 and S8 were selected in order to compare the reference geometry with one proposed TPMS topology. The software used to obtain the comparison is Inspire (Hexagon-Sweden). The deviation distributions show that most of the points are within the imposed tolerance, with root mean squares of the values of 0.032 and 0.039 mm. The imposed threshold was exceeded generally on the surfaces of the fastening elements and in the lower area where the part was in contact with the side supports, and their removal was not carried out with good enough precision (red color). Isolated cases were obtained for S8 of deviations inside the sample with a maximum value of 0.119 mm.
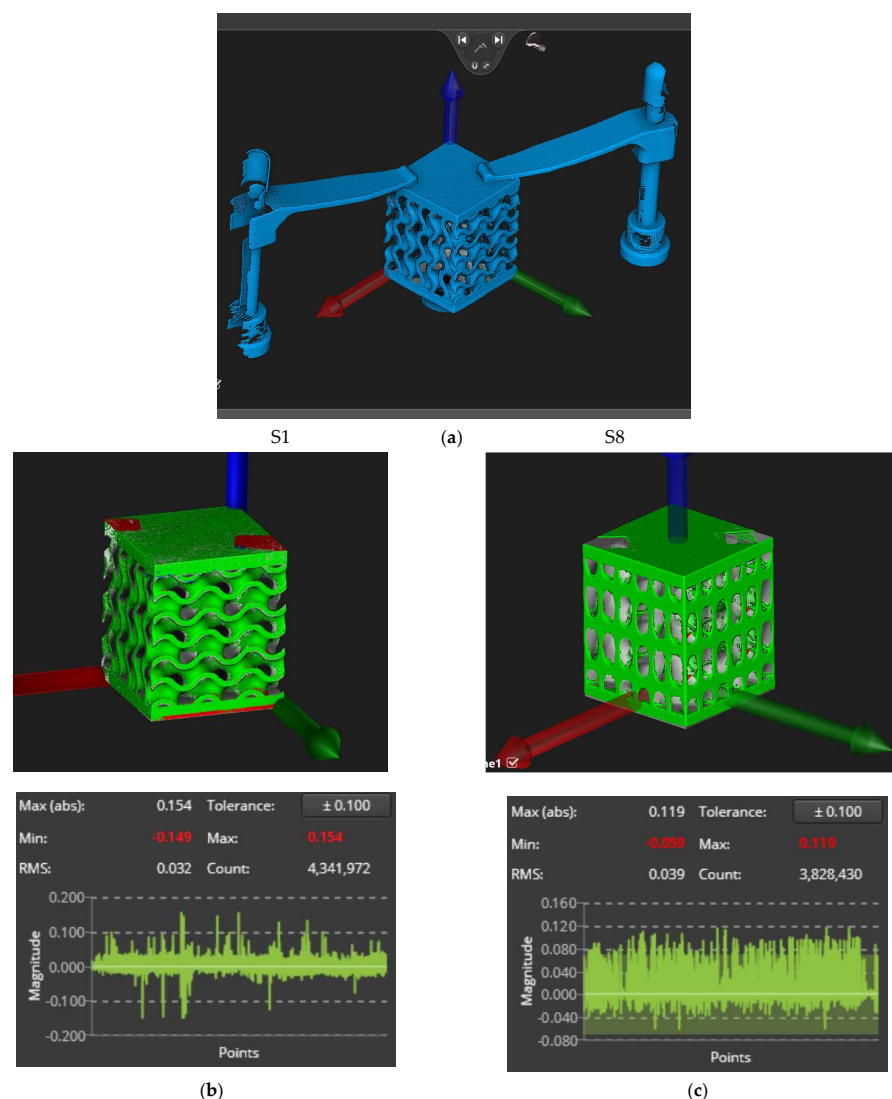


**Figure 7.** Results of 3D inspection: (**a**) Example of generated point cloud for S1 and S8; (**b**) Geometric deviations resulted for S1; (**c**) Geometric deviations resulted for S8.

### 3.3. Roughness Analysis

The results obtained from the roughness analysis are presented in Table 3. For each pass, the values for the standard parameters $R_a$ (arithmetic mean deviation of the profile within the evaluation length), $R_t$ (distance between the highest and lowest point of the

profile), $R_p$ (distance between the highest point and the mean line of the profile), and $R_v$ (distance between the lowest point and the mean line of the profile) were calculated.

**Table 3.** Results obtained through the roughness analysis. All values are given in the order denoted by the numbering of the 10 topologies (first row S1–S5, second row S6–S10).

| Parameter | Bottom Surface Passes | | | | | Sidewall Passes | | | | | Upper Surface Passes | | | | |
|---|---|---|---|---|---|---|---|---|---|---|---|---|---|---|---|
| Rugozity $R_a$ [μm] | 2.7 | 4.0 | 5.5 | 2.8 | 3.0 | 1.8 | 2.2 | 1.5 | 1.8 | 2.2 | 1.1 | 1.2 | 10.6 | 0.8 | 1.0 |
| | 3.0 | 3.1 | 2.9 | 3.2 | 2.7 | 2.6 | 2.0 | 2.6 | 0.9 | 3.6 | 1.7 | 0.8 | 0.7 | 0.7 | 0.7 |
| | Average 3.28 | | | | | Average 2.12 | | | | | Average 1.93 | | | | |
| $R_t$ [μm] | 23.0 | 35.5 | 67.5 | 25.5 | 27.0 | 16.5 | 16.5 | 23.0 | 18.0 | 23.0 | 27.1 | 16.0 | 160.5 | 14.0 | 19.0 |
| | 26.0 | 26.0 | 23.0 | 22.5 | 22.0 | 20.5 | 19.0 | 28.0 | 20.5 | 31.0 | 27.5 | 11.5 | 8.5 | 6.5 | 13.0 |
| | Average 29.80 | | | | | Average 21.60 | | | | | Average 27.56 | | | | |
| $R_v$ [μm] | 7.0 | 11.5 | 19.0 | 9.5 | 8.5 | 5.0 | 5.5 | 4.5 | 5.5 | 5.5 | 6.5 | 7.0 | 4.5 | 6.5 | 7.5 |
| | 9.5 | 9.5 | 8.5 | 9.0 | 7.0 | 6.0 | 5.0 | 8.5 | 3.0 | 9.5 | 8.0 | 6.5 | 9.5 | 3.5 | 9.5 |
| | Average 9.90 | | | | | Average 5.80 | | | | | Average 6.90 | | | | |
| $R_p$ [μm] | 8.0 | 11.0 | 13.5 | 8.5 | 9.5 | 6.5 | 7.0 | 4.5 | 6.5 | 7.5 | 4.7 | 5.0 | 20.5 | 4.5 | 4.5 |
| | 10.0 | 9.5 | 8.0 | 9.0 | 8.0 | 8.0 | 6.5 | 8.5 | 3.5 | 9.5 | 10.5 | 4.5 | 3.0 | 2.5 | 4.5 |
| | Average 9.50 | | | | | Average 6.80 | | | | | Average 6.42 | | | | |

The values presented in Table 3 represent the highest value identified for each specimen and the average for each type of surface. A good indicator of the quality of the surfaces is the small variation in the calculated parameters among all the samples. Sample S3 has a higher roughness on the upper surface passes due to capturing a superficial scratch, thus having the highest values for $R_a$ and $R_t$, 10.6 μm, respectively, 160.5 μm. As expected, sample S10 has the highest rigidity on the sidewall passes, which means that the struts of the stochastic sample have a worse surface quality than the thin walls of the TPMS geometries. The surface with the lowest roughness is the one in contact with the printing surface, given its purpose of allowing parts to be supported throughout the printing process. This is followed by the top and side surfaces, where no defects are identified at the separation zones between the layers. We note that the $R_a$ roughness values of the tested samples fall within the range of average values specific to SLA procedures, 0.87–4.44 μm [38]. As a reference, the values of machining procedures have an average roughness of 2.32–2.57 μm.

Figure 8 presents an example of a line roughness analysis across a superficial scratch resulting from sample handling. The red line indicates the length of 2.7 mm on which the analysis was performed with a roughness value of 3.07 μm and a height difference of 13.64 μm. Multiple surfaces and verification lines were considered, with no significant outliers being identified.
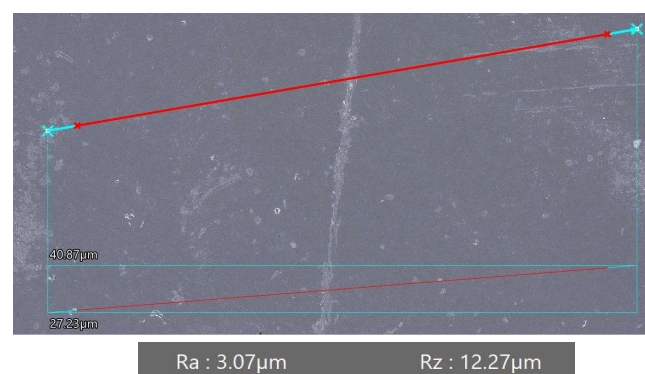


Ra : 3.07μm          Rz : 12.27μm

**Figure 8.** Roughness analysis using Keyence VHX-7100.

### 3.4. Defect Inspection

For a more thorough surface analysis, the microscope inspection was also used to detect defects and their nature, to identify the reasons why they occurred, and ways to isolate them. Figure 9 shows examples of defects discovered during surface analysis. The scale is different in the images in order to best capture the defects and is represented in the bottom right corner. Figure 9a shows a small resin micro-exfoliation on the surface, which does not, however, present a danger of entire layer exfoliation.
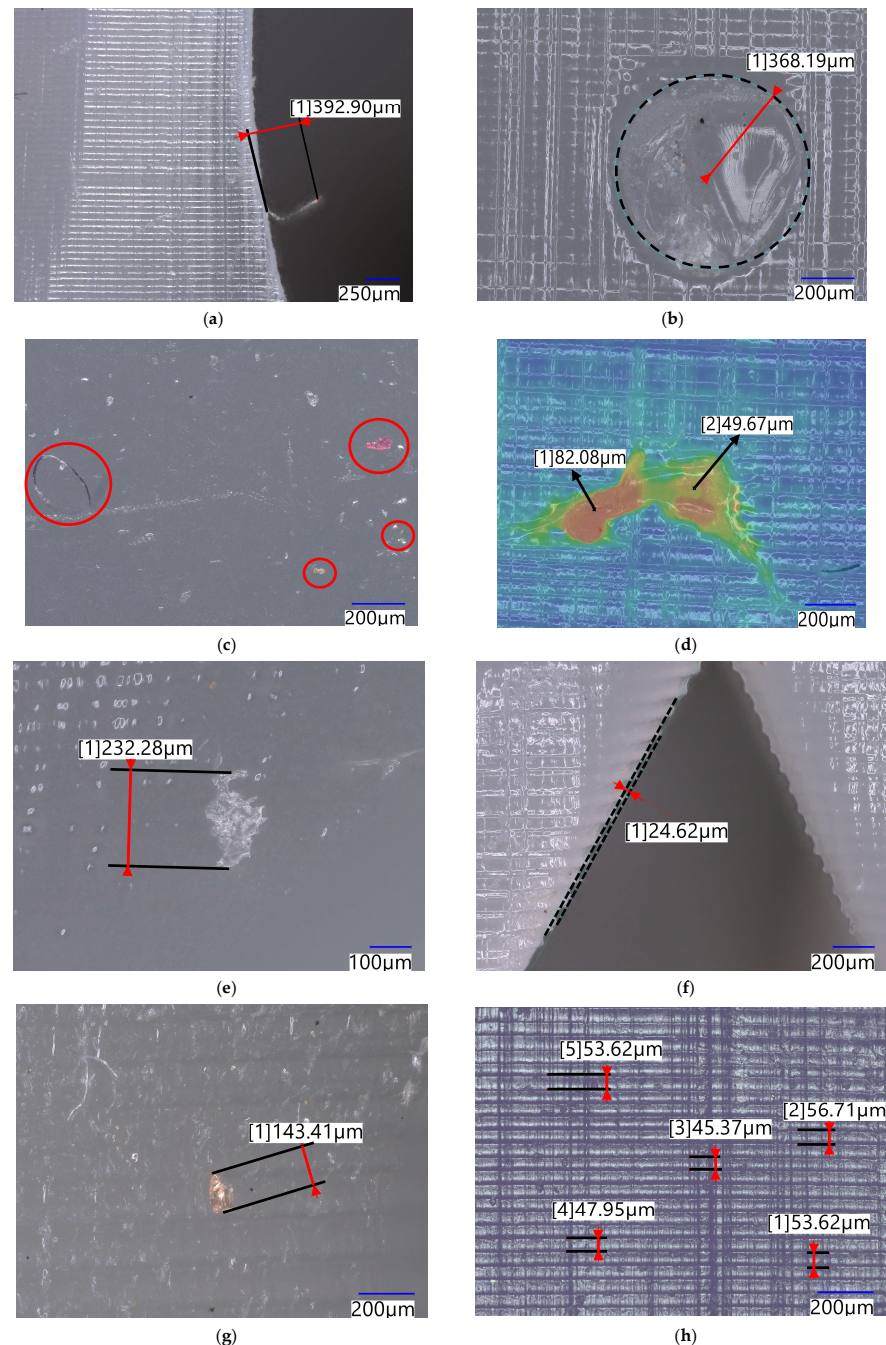


**Figure 9.** Defects identified under microscopic inspection: (**a**) micro-exfoliation; (**b**) trace left by lateral support removal; (**c**) resin contamination; (**d**) polymerization defect; (**e**) excess polymerization micro-irregularity; (**f**) dimensional surface deviation; (**g**) surface contaminant; (**h**) uniform layer-by-layer aspect.

Figure 9b displays a trace left in the contact area with the lateral printing supports after removing them. It can be noticed that the 0.35 mm predefined dimension of the supports is in good accordance with the dimension of the mark. In this case, the difference in light reflection was not caused by a hole or a protuberance of the circular area, but by a difference in roughness caused by the fracture of the support. Figure 9c shows impurities that can be found embedded in the sample due to their presence in the resin or its improper storage. Figure 9d shows a polymerization defect, where excess resin is cured on the surface, leading to dimensional deviations. The color scale visible in the image displays the height of the surface profile, with blue representing the base plane of the specimen and red indicating points that are different from the theoretical expected value. Two measurements are specified in the image, representing the height of the points compared to the base plane of the surface. Even though the 0.1 mm tolerance is not exceeded, such polymerization defects are critical because they show that the shape of the part can effectively be modified in ways that can alter the geometry of the samples. A similar defect is present in Figure 9e, where another polymerization defect is highlighted. This, however, is not entirely attached to the sample, meaning that it could be either generated by resin, which should have been part of the specimen and is now out of place, or is just excessively cured resin out of the sample's boundary. Figure 9f indicates surface micro-irregularities that appeared during printing. This phenomenon was better visible in the stochastically defined sample, S10, and it is due to the fact that the random definition does not provide accurate enough resolution for the parts contour. The dimensional deviation is however small, being generally half the layer thickness, as seen in the measurement visible in the image. In the image presented in Figure 9g, a grain of sand can be noticed left on the surface after a water jet cutting process has been applied, thus representing a defect unrelated to the manufacturing method. Taking into account all these identified defects, the conclusion is that the printing accuracy is good with no major defects that could endanger the integrity of the specimens. This is also suggested by the lack of any porosities or unevenness between the printed layers, very easily identified by the horizontal lines in Figure 9h. The thickness layer is also visible in the measurements, with small deviations from the expected thickness of 50 μm.

### 3.5. Homogeneity Inspection

During the ultrasound testing presented before, no situation was observed where the thickness of the flat surfaces analyzed differed significantly from the nominal ones. To have a better indication of the homogeneity of the samples, a direct comparison between the lateral surfaces (Figure 10a,c) and the inner surfaces exposed through water jet cutting (Figure 10b,d) is presented below. The magnification is increased from 40× in the first row of pictures to 200× in the second row, while the images were modified to remove light reflections in order to get a better view of the surface texture.

A first observation is the disappearance of the layer-by-layer aspect inside the samples, which indicates optimal homogenization during printing. This aspect is preserved at the outer contour of the part due to the lower temperatures and printing precision. Analyzing the two types of surfaces, it is found that there are no impurities in the mass of the piece or insufficiently polymerized areas. At a higher magnification of 200×, microscopic cavities can be identified as darker spots in Figure 10d. When trying to achieve a better local focus of the image, the difference in light reflectivity is an indicator that the cavity was caused by material tearing at the time of cutting rather than a locally unpolymerized area. Still, while the specimens present in most parts of their volume have a homogeneous appearance, there are suspicions regarding the possibility of finding areas with porosity.
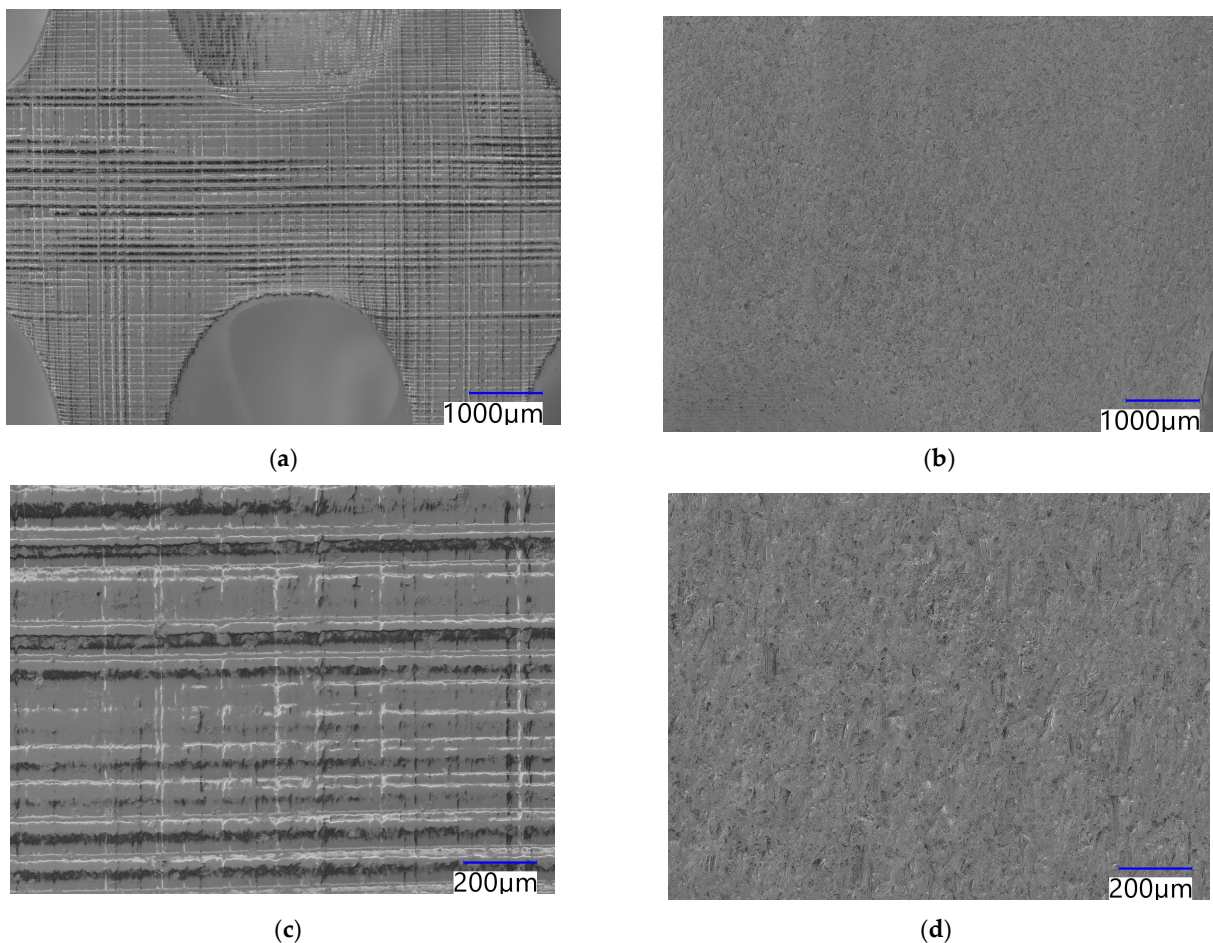
(**a**)



(**b**)



(**c**)



(**d**)

**Figure 10.** Microscopic images: (**a**) lateral surface of the sample—40× magnification; (**b**) cross-section exposed by cutting the samples—40× magnification; (**c**) lateral surfaces of the samples—200× magnification; (**d**) cross-section exposed by cutting the samples—200× magnification.

## 4. Discussion

After sample fabrication, a discrepancy was determined regarding the density of the resin after polymerization, thus having a higher value of 1.21 g/cm$^3$, compared to the value declared by the manufacturer of 1.07 g/cm$^3$. Most likely, the value is related to the uncured liquid resin, and the difference in density is associated with a tighter molecular structure of the cured parts. Such a difference has been signaled in relevant literature such as [39,40] or specified by other resin producers [41]. A direct relationship between maximum external surface area and deviation from average sample mass was also determined, indicating that parts with complex geometries and features with small dimensions should undergo intensive washing treatments. This is necessary to successfully remove the entire mass of resin that has adhered to the surface of the part before it is post-processed in the curing chamber.

Through 3D scanning of the manufactured samples, it was established that there are no significant deviations from the designed CAD geometry. The only dimensions out of the considered 0.1 mm tolerance were the lower areas where parts came into contact with the plate, which supports the side supports. This can be eliminated by changing the printing settings to force a greater distance between the components or by omitting the support plate altogether. Dimensional deviations were similar to the ones specified in other publications, where the average difference from the nominal values ranged between 0.40 mm and 0.15 mm [42] or from 0.42 mm to 0.127 mm [43]. Emir et al. also stated in [44] that the average dimensional deviations of an SLA technique have a value of 68.5 μm.

By analyzing the roughness of the flat surfaces of the samples, it was determined that the same type of surfaces showed very close roughness values, which denotes a stable manufacturing process without fluctuations. The roughness values validated the results previously obtained in the dimensional analysis, as there were no found values of $R_p$ above the tolerated limit of 0.1 mm. The average roughness $R_a$ was 2.47 μm, a value specific to well-controlled additive manufacturing processes, and the average distance between the highest and lowest point of the profiles $R_t$ was measured as 160.5 μm. These values indicate the very good quality of the surfaces and the lack of obvious layer-by-layer appearance; therefore, a good homogeneity of the part was obtained without the need for additional grinding or post-processing techniques. The values obtained for roughness ($R_a$) are consistent with relevant studies on the same topic, such as the ones specified in [38]: 0.87–4.44 μm, in [45]: 0.71–2.91 μm, or in [46]: 2.66—3.37 μm. This, however, can be improved as different papers suggest smaller roughness values.

A further analysis of the surface quality involved a microscopic analysis of the specimens. Most of the analyzed surfaces showed no defects, reinforcing the idea that the chosen manufacturing process is suitable for the designed geometry. Different types of possible surface defects were highlighted, some of which can be addressed by careful control of how the resin is stored between successive prints. Also, an important aspect of avoiding damage to the parts is suggested to be a very thorough cleaning of any residual resin from the specimens because it is adherent and tends to accumulate impurities. Furthermore, careful handling of the samples before they are introduced into the UV treatment enclosure can alleviate the problems of superficial surface defects.

To analyze the internal defects of the specimens, a nondestructive method using ultrasonic waves was employed. Flat surfaces large enough to allow probe contact were examined, with no indication of in-depth defects. This test method ruled out the presence of major defects, such as exfoliation or internal voids. However, to check for very small porosities that cannot be captured by non-destructive methods, an inner volume analysis of the samples was conducted. The parts were sectioned by water jet cutting, and the newly generated surfaces were analyzed. By comparing them with the side surfaces, a better homogeneity in the depth of the parts was identified, along with a lack of a layer-by-layer aspect that is still visible under the microscope on the outside surface. The absence of inclusions of other materials may indicate that the impurities on the outer surface are not a consequence of improper storage but rather of inadequate post-processing prior to curing. Among the numerous surfaces checked, there was also evidence of micro indentations in the processed surfaces, which may indicate either internal voids, insufficiently polymerized areas that were removed during cutting, or a consequence of an improper cutting process. Regardless of the cause, there are indications of possible local micro-inhomogeneities, which would be better identified in further analysis by subjecting the samples to an X-ray computed tomography inspection.

Thus, the results suggest that the SLA technique and material employed in this study are suitable for fabricating TPMS structures with good accuracy and homogeneity. In order to evaluate the repeatability and stability of the fabrication process, multiple samples were fabricated for each proposed topology, and their compressive response was evaluated. A maximum deviation of 11% between the stress-strain curves was visible on the stochastic geometry, while only a maximum of 7% was achieved among the TPMS samples (S8). This was however attributed to an insufficient control of the time between the fabrication and the post-processing stages and not on the fabrication quality of the samples. A further analysis of this will be presented in future research.

**Institutional Review Board Statement:** Not applicable.

**Informed Consent Statement:** Not applicable.

**Data Availability Statement:** The raw data supporting the conclusions of this article will be made available by the authors upon request.

**Conflicts of Interest:** The authors declare no conflicts of interest.

## References

1. Zhou, H.; Zhao, M.; He, N.; Zhang, T.; Ma, X.; Zhang, D.Z. Compressive Response and Energy Absorption of Additive Manufactured Ti-6Al-4V Triply Periodic Minimal Surface Honeycomb Structure. *J. Alloys Compd.* **2024**, *982*, 173744. [CrossRef]
2. Al-Ketan, O.; Rowshan, R.; Palazotto, A.N.; Abu Al-Rub, R.K. On Mechanical Properties of Cellular Steel Solids with Shell-Like Periodic Architectures Fabricated by Selective Laser Sintering. *J. Eng. Mater. Technol. Trans. ASME* **2019**, *141*, 021009. [CrossRef]
3. Al-Ketan, O.; Rowshan, R.; Abu Al-Rub, R.K. Topology-Mechanical Property Relationship of 3D Printed Strut, Skeletal, and Sheet Based Periodic Metallic Cellular Materials. *Addit. Manuf.* **2018**, *19*, 167–183. [CrossRef]
4. Abueidda, D.W.; Elhebeary, M.; Shiang, C.S.; Pang, S.; Abu Al-Rub, R.K.; Jasiuk, I.M. Mechanical Properties of 3D Printed Polymeric Gyroid Cellular Structures: Experimental and Finite Element Study. *Mater. Des.* **2019**, *165*, 107597. [CrossRef]
5. Araya, M.; Jaskari, M.; Rautio, T.; Guillén, T.; Järvenpää, A. Assessing the Compressive and Tensile Properties of TPMS-Gyroid and Stochastic Ti64 Lattice Structures: A Study on Laser Powder Bed Fusion Manufacturing for Biomedical Implants. *J. Sci. Adv. Mater. Devices* **2024**, *9*, 100663. [CrossRef]
6. Gabrieli, R.; Wenger, R.; Mazza, M.; Verné, E.; Baino, F. Design, Stereolithographic 3D Printing, and Characterization of TPMS Scaffolds. *Materials* **2024**, *17*, 654. [CrossRef]
7. Ataee, A.; Li, Y.; Wen, C. A Comparative Study on the Nanoindentation Behavior, Wear Resistance and in Vitro Biocompatibility of SLM Manufactured CP–Ti and EBM Manufactured Ti64 Gyroid Scaffolds. *Acta Biomater.* **2019**, *97*, 587–596. [CrossRef]
8. Cresswell, N.D.; Ameri, A.A.H.; Wang, J.; Wang, H.; Hazell, P.; Escobedo-Diaz, J.P. Characterization and Modelling of Triply Periodic Minimum Surface (TPMS) Lattice Structures for Energy Absorption in Automotive Applications. In *Characterization of Minerals, Metals, and Materials 2024*; Springer: Berlin/Heidelberg, Germany, 2024; pp. 295–305. [CrossRef]
9. Zhang, L.; Feih, S.; Daynes, S.; Chang, S.; Wang, M.Y.; Wei, J.; Lu, W.F. Energy Absorption Characteristics of Metallic Triply Periodic Minimal Surface Sheet Structures under Compressive Loading. *Addit. Manuf.* **2018**, *23*, 505–515. [CrossRef]
10. Feng, J.; Fu, J.; Yao, X.; He, Y. Triply Periodic Minimal Surface (TPMS) Porous Structures: From Multi-Scale Design, Precise Additive Manufacturing to Multidisciplinary Applications. *Int. J. Extrem. Manuf.* **2022**, *4*, 022001. [CrossRef]
11. Al-Ketan, O.; Lee, D.W.; Rowshan, R.; Abu Al-Rub, R.K. Functionally Graded and Multi-Morphology Sheet TPMS Lattices: Design, Manufacturing, and Mechanical Properties. *J. Mech. Behav. Biomed. Mater.* **2020**, *102*, 103520. [CrossRef]
12. Sang, L.; Wu, W.; Sun, Z.; Wang, F.; Xu, J.; Tian, J.; Zhao, Y.; Zhang, H. Reusability and Energy Absorption Behavior of 4D-Printed Heterogeneous Lattice Structures Based on Biomass Shape Memory Polyester. *J. Mater. Res. Technol.* **2023**, *27*, 1563–1578. [CrossRef]
13. Jin, J.; Wu, S.; Yang, L.; Zhang, C.; Li, Y.; Cai, C.; Yan, C.; Shi, Y. Ni–Ti Multicell Interlacing Gyroid Lattice Structures with Ultra-High Hyperelastic Response Fabricated by Laser Powder Bed Fusion. *Int. J. Mach. Tools Manuf.* **2024**, *195*, 104099. [CrossRef]
14. Ormiston, S.; Srinivas Sundarram, S. Fiberglass-Reinforced Triply Periodic Minimal Surfaces (TPMS) Lattice Structures for Energy Absorption Applications. *Polym. Compos.* **2024**, *45*, 523–534. [CrossRef]
15. Novak, N.; Borovinšek, M.; Al-Ketan, O.; Ren, Z.; Vesenjak, M. Impact and Blast Resistance of Uniform and Graded Sandwich Panels with TPMS Cellular Structures. *Compos. Struct.* **2022**, *300*, 116174. [CrossRef]
16. Song, J.; Wang, M.; Li, D.; Zhang, J. Deformation and Energy Absorption Performance of Functionally Graded TPMS Structures Fabricated by Selective Laser Melting. *Appl. Sci.* **2024**, *14*, 2064. [CrossRef]
17. Novak, N.; Al-Ketan, O.; Krstulović-Opara, L.; Rowshan, R.; Abu Al-Rub, R.K.; Vesenjak, M.; Ren, Z. Quasi-Static and Dynamic Compressive Behaviour of Sheet TPMS Cellular Structures. *Compos. Struct.* **2021**, *266*, 113801. [CrossRef]
18. Mishra, A.K.; Kumar, A. Compression Behavior of Triply Periodic Minimal Surface Polymer Lattice Structures. *Exp. Mech.* **2023**, *63*, 609–620. [CrossRef]
19. Miralbes, R.; Ranz, D.; Pascual, F.J.; Zouzias, D.; Maza, M. Characterization of Additively Manufactured Triply Periodic Minimal Surface Structures under Compressive Loading. *Mech. Adv. Mater. Struct.* **2022**, *29*, 1841–1855. [CrossRef]
20. Khan, S.Z.; Masood, S.H.; Ibrahim, E.; Ahmad, Z. Compressive Behaviour of Neovius Triply Periodic Minimal Surface Cellular Structure Manufactured by Fused Deposition Modelling. *Virtual Phys. Prototyp.* **2019**, *14*, 360–370. [CrossRef]
21. Abueidda, D.W.; Elhebeary, M.; Shiang, C.S.; Abu Al-Rub, R.K.; Jasiuk, I.M. Compression and Buckling of Microarchitectured Neovius-Lattice. *Extrem. Mech. Lett.* **2020**, *37*, 100688. [CrossRef]
22. Nazir, A.; Hussain, S.; Ali, H.M.; Waqar, S. Design and Mechanical Performance of Nature-Inspired Novel Hybrid Triply Periodic Minimal Surface Lattice Structures Fabricated Using Material Extrusion. *Mater. Today Commun.* **2024**, *38*, 108349. [CrossRef]

23. Chen, Y.; Peng, X.; Kong, L.; Dong, G.; Remani, A.; Leach, R. Defect Inspection Technologies for Additive Manufacturing. *Int. J. Extrem. Manuf.* **2021**, *3*, 022002. [CrossRef]

24. Segovia Ramírez, I.; García Márquez, F.P.; Papaelias, M. Review on Additive Manufacturing and Non-Destructive Testing. *J. Manuf. Syst.* **2023**, *66*, 260–286. [CrossRef]

25. Charalampous, P.; Kostavelis, I.; Tzovaras, D. Non-Destructive Quality Control Methods in Additive Manufacturing: A Survey. *Rapid Prototyp. J.* **2020**, *26*, 777–790. [CrossRef]

26. Frazier, W.E. Metal Additive Manufacturing: A Review. *J. Mater. Eng. Perform.* **2014**, *23*, 1917–1928. [CrossRef]

27. Khanafer, K.; Cao, J.; Kokash, H. Condition Monitoring in Additive Manufacturing: A Critical Review of Different Approaches. *J. Manuf. Mater. Process.* **2024**, *8*, 95. [CrossRef]

28. Thompson, M.K.; Moroni, G.; Vaneker, T.; Fadel, G.; Campbell, R.I.; Gibson, I.; Bernard, A.; Schulz, J.; Graf, P.; Ahuja, B.; et al. Design for Additive Manufacturing: Trends, Opportunities, Considerations, and Constraints. *CIRP Ann.* **2016**, *65*, 737–760. [CrossRef]

29. Abdelrahman, M.; Reutzel, E.W.; Nassar, A.R.; Starr, T.L. Flaw Detection in Powder Bed Fusion Using Optical Imaging. *Addit. Manuf.* **2017**, *15*, 1–11. [CrossRef]

30. Vera-Rodríguez, G.; Moreno-Corrales, L.; Marín-González, I.; Barba, D.; Montáns, F.J.; Sanz-Gómez, M.Á. Incorporation of Defects in Finite Elements to Model Effective Mechanical Properties of Metamaterial Cells Printed by Selective Laser Melting. *Sustainability* **2024**, *16*, 1167. [CrossRef]

31. Dastani, K.; Movahhedy, M.R.; Yu, H.; Khodaygan, S.; Zhang, L.; Wang, M.Y. Effect of Geometric Deviations on the Strength of Additively Manufactured Ultralight Periodic Shell-Based Lattices. *Eng. Fail. Anal.* **2023**, *150*, 107328. [CrossRef]

32. Engineering, Design, and Simulation Software | NTop. Available online: https://www.ntop.com/software/products/ (accessed on 31 August 2023).

33. Jones, A.; Leary, M.; Bateman, S.; Easton, M. TPMS Designer: A Tool for Generating and Analyzing Triply Periodic Minimal Surfaces. *Softw. Impacts* **2021**, *10*, 100167. [CrossRef]

34. Vasile, A.; Constantinescu, D.M.; Coropețchi, I.C.; Sorohan, Ș.; Apostol, D.A. Definition, Fabrication, and Compression Testing of Sandwich Structures with Novel TPMS-Based Cores. *Materials* **2024**, *17*, 5150. [CrossRef] [PubMed]

35. de Pastre, M.A.; Quinsat, Y.; Lartigue, C. Effects of Additive Manufacturing Processes on Part Defects and Properties: A Classification Review. *Int. J. Interact. Des. Manuf. (IJIDeM)* **2022**, *16*, 1471–1496. [CrossRef]

36. Rico-Baeza, G.; Cuan-Urquizo, E.; Pérez-Soto, G.I.; Alcaraz-Caracheo, L.A.; Camarillo-Gómez, K.A. Additively Manufactured Lattice Materials with a Double Level of Gradation: A Comparison of Their Compressive Properties When Fabricated with Material Extrusion and Vat Photopolymerization Processes. *Materials* **2023**, *16*, 649. [CrossRef]

37. Guerra Silva, R.; Torres, M.J.; Zahr Viñuela, J. A Comparison of Miniature Lattice Structures Produced by Material Extrusion and Vat Photopolymerization Additive Manufacturing. *Polymers* **2021**, *13*, 2163. [CrossRef]

38. Arnold, C.; Monsees, D.; Hey, J.; Schweyen, R. Surface Quality of 3D-Printed Models as a Function of Various Printing Parameters. *Materials* **2019**, *12*, 1970. [CrossRef]

39. Ni, R.; Qian, B.; Liu, C.; Liu, X.; Qiu, J. A Cross-Linking Strategy with Moderated Pre-Polymerization of Resin for Stereolithography. *RSC Adv.* **2018**, *8*, 29583–29588. [CrossRef]

40. Ren, M.; Wang, L.; Li, T.; Wei, B. Molecular Investigation on the Compatibility of Epoxy Resin with Liquid Oxygen. *Theor. Appl. Mech. Lett.* **2020**, *10*, 38–45. [CrossRef]

41. Solid Density of 3D-Printed Resin Parts. Available online: https://www.liqcreate.com/supportarticles/solid-density-of-3d-printed-resin-parts-after-post-processing/ (accessed on 28 November 2024).

42. Mukhangaliyeva, A.; Dairabayeva, D.; Perveen, A.; Talamona, D. Optimization of Dimensional Accuracy and Surface Roughness of SLA Patterns and SLA-Based IC Components. *Polymers* **2023**, *15*, 4038. [CrossRef]

43. Mukhtarkhanov, M.; Perveen, A.; Talamona, D. Application of Stereolithography Based 3D Printing Technology in Investment Casting. *Micromachines* **2020**, *11*, 946. [CrossRef]

44. Emir, F.; Ayyildiz, S. Accuracy Evaluation of Complete-Arch Models Manufactured by Three Different 3D Printing Technologies: A Three-Dimensional Analysis. *J. Prosthodont. Res.* **2021**, *65*, 365–370. [CrossRef] [PubMed]

45. Lu, Y.; Wang, L.; Dal Piva, A.M.O.; Tribst, J.P.M.; Nedeljkovic, I.; Kleverlaan, C.J.; Feilzer, A.J. Influence of Surface Finishing and Printing Layer Orientation on Surface Roughness and Flexural Strength of Stereolithography-Manufactured Dental Zirconia. *J. Mech. Behav. Biomed. Mater.* **2023**, *143*, 105944. [CrossRef] [PubMed]

46. Zheng, X.; Duan, F.; Song, Z.; Mo, H.; Li, Z.; Song, Y.; Su, Y.; Wang, X. A TMPS-Designed Personalized Mandibular Scaffolds with Optimized SLA Parameters and Mechanical Properties. *Front. Mater.* **2022**, *9*, 966031. [CrossRef]